The conical shape of DIM lipids promotes *Mycobacterium tuberculosis* infection of macrophages

Jacques Augenstreich[a,1,2], Evert Haanappel[a,1], Guillaume Ferré[a], Georges Czaplicki[a], Franck Jolibois[b], Nicolas Destainville[c], Christophe Guilhot[a], Alain Milon[a,3], Catherine Astarie-Dequeker[a,3], and Matthieu Chavent[a,3]

[a]Institut de Pharmacologie et de Biologie Structurale, Université de Toulouse, CNRS, Université Paul Sabatier, 31400 Toulouse, France; [b]Laboratoire de Physique et Chimie des Nano-objets, Institut National des Sciences Appliquées, Université de Toulouse, CNRS, Université Paul Sabatier, F-31077 Toulouse, France; and [c]Laboratoire de Physique Théorique, Institut de Recherche sur les Systèmes Atomiques et Moléculaires Complexes, Université de Toulouse, CNRS, Université Paul Sabatier, 31062 Toulouse, France

Edited by Michael L. Klein, Temple University, Philadelphia, PA, and approved October 22, 2019 (received for review June 17, 2019)

Phthiocerol dimycocerosate (DIM) is a major virulence factor of the pathogen *Mycobacterium tuberculosis* (*Mtb*). While this lipid promotes the entry of *Mtb* into macrophages, which occurs via phagocytosis, its molecular mechanism of action is unknown. Here, we combined biophysical, cell biology, and modeling approaches to reveal the molecular mechanism of DIM action on macrophage membranes leading to the first step of *Mtb* infection. Matrix-assisted laser desorption ionization time-of-flight (MALDI-TOF) mass spectrometry showed that DIM molecules are transferred from the *Mtb* envelope to macrophage membranes during infection. Multiscale molecular modeling and ^{31}P-NMR experiments revealed that DIM adopts a conical shape in membranes and aggregates in the stalks formed between 2 opposing lipid bilayers. Infection of macrophages pretreated with lipids of various shapes uncovered a general role for conical lipids in promoting phagocytosis. Taken together, these results reveal how the molecular shape of a mycobacterial lipid can modulate the biological response of macrophages.

mycobacterial lipids shape | nonbilayer membrane structure | multiscale molecular dynamics | solid-state NMR | macrophage infection

Phthiocerol dimycocerosates (DIMs/PDIMs) are highly hydrophobic lipids containing 2 multiple methyl-branched fatty acid chains (Fig. 1*A*). These lipids are mostly found in the cell wall of pathogenic mycobacteria and are particularly abundant in *Mycobacterium tuberculosis* (*Mtb*) (1), the causative agent of tuberculosis. They constitute one of the main *Mtb* virulence factors (2). Indeed, *Mtb* strains lacking DIM are drastically attenuated (3) and are more likely to be killed by the early pulmonary innate immune response (4) when the bacteria encounter macrophages. Recent work has revealed that DIMs modulate macrophage metabolism (5) and immune functions (6, 7). In particular, DIMs increase the ability of *Mtb* to infect macrophages by modulating phagocytosis (8), a fundamental immune process involving membrane remodeling. However, how DIMs intervene in these cellular processes remains poorly understood.

Mtb synthesizes a large variety of lipid virulence factors, most of which are amphipathic glycolipids. These glycolipids act through their saccharide domains as potential ligands for membrane receptors on macrophages to induce *Mtb* phagocytosis (9). Lacking a saccharide moiety, DIM cannot engage in such interactions. In contrast, the molecular mechanism involving DIM may be related to a global effect on the physical properties of the host cell membrane, such as its fluidity and organization (8). Modifying such properties can be a successful strategy for bacteria to modulate eukaryotic cell functions. Several types of pathogenic mycobacteria apply this strategy to influence the fate of their host cells. For example, *Mycobacterium ulcerans* produces the lipid-like endotoxin mycolactone, which interacts with host membranes and disturbs their lipid organization (10). In addition, pathogenic mycobacteria use lipoarabinomannan to enter neutrophils and prevent phagolysosome formation (11).

The biophysical properties of DIM in biological membranes have not yet been characterized at the molecular level. In particular, it is unclear if such a complex and large lipid can be incorporated in a simple phospholipid bilayer and what shape DIM must adopt in such a membrane. The shape of lipid molecules, determined by structural properties (12) like their head group size, acyl chain lengths, and degrees of acyl chain unsaturation, can drastically affect the structure and organization of biological membranes (13, 14). Studying how the molecular shape of lipids may disorganize lipid bilayers and how this can be related to biological function is still a challenge (15). It requires linking the structure of molecules and their biophysical actions at the nanoscale to macroscopic consequences on the cell functions. To achieve this for DIM, we developed a multidisciplinary approach combining multiscale molecular dynamics (MD) simulations, solid-state NMR, and cell biology experiments. This revealed how the molecular shape of DIM can affect macrophage membranes to promote phagocytosis.

Results

DIMs Are Transferred to Host Cell Membranes during Macrophage Infection. First, we used matrix-assisted laser desorption ionization time-of-flight (MALDI-TOF) mass spectrometry to assess

Significance

Phthiocerol dimycocerosates (DIMs) are characteristic lipids present in the envelope of *Mycobacterium tuberculosis* (*Mtb*), the causative agent of tuberculosis, and other pathogenic mycobacteria. Due to the very hydrophobic nature of DIM and the difficulty of working with such pathogenic bacteria, these lipids are especially difficult to study. Based on a multidisciplinary research strategy involving mass spectrometry, solid-state NMR, multiscale modeling, and cell biology, we discovered how the conical shape of DIM lipids modulates macrophage phagocytosis of *Mtb*. These results provide insights into the biophysical action of *Mtb* lipid virulence factors on macrophage membranes and how this mechanism can modulate the regulation of macrophage phagocytosis.

Author contributions: E.H., A.M., C.A.-D., and M.C. designed research; J.A., E.H., G.C., F.J., N.D., A.M., C.A.-D., and M.C. performed research; J.A., E.H., G.F., F.J., N.D., A.M., C.A.-D., and M.C. analyzed data; and J.A., E.H., G.F., G.C., F.J., N.D., C.G., A.M., C.A.-D., and M.C. wrote the paper.

The authors declare no competing interest.

This article is a PNAS Direct Submission.

Published under the PNAS license.

Data deposition: MD simulation material and scripts, as well as tables for NMR phase transitions, are available at https://github.com/MChavent/DIM_data.

[1]J.A. and E.H. contributed equally to this work.

[2]Present address: Department of Cell Biology & Molecular Genetics, College of Computer, Mathematical, & Natural Sciences, University of Maryland, College Park, MD 20742-4451.

[3]To whom correspondence may be addressed. Email: alain.milon@ipbs.fr, catherine.astarie-dequeker@ipbs.fr, or matthieu.chavent@ipbs.fr.

This article contains supporting information online at https://www.pnas.org/lookup/suppl/doi:10.1073/pnas.1910368116/-/DCSupplemental.

Downloaded at UNIVERSITAT MUENCHEN Bibliothek Bereich Physiologie on November 24, 2019

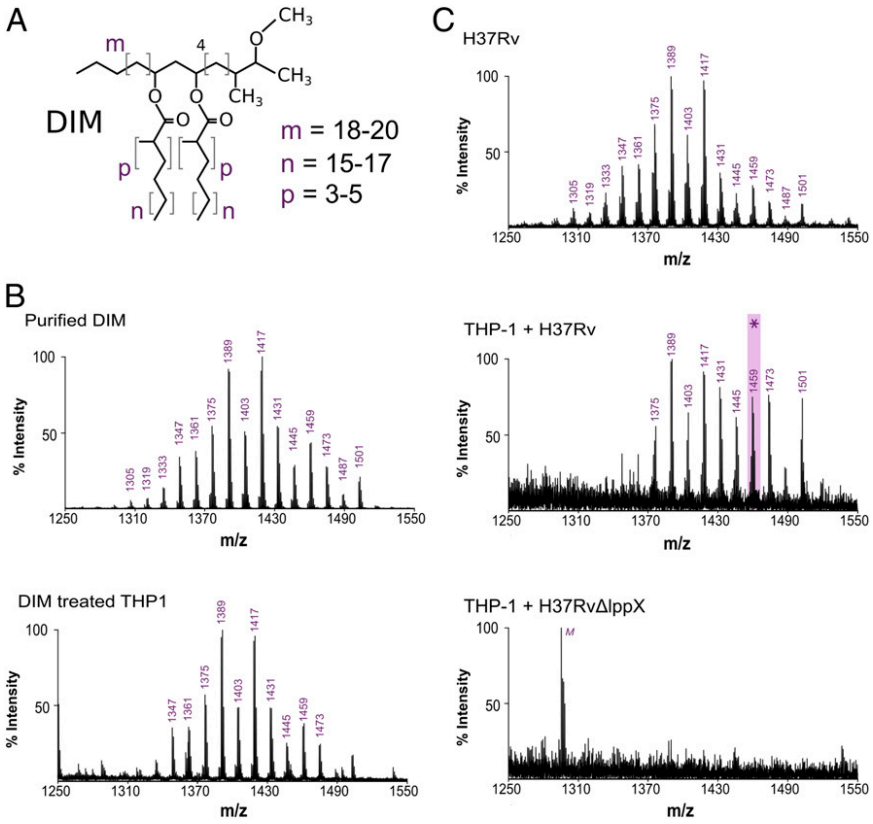

Fig. 1. DIMs are transferred from the bacterial envelope to macrophage membranes. (*A*) Structure of the DIM family of lipids, where m denotes the range of carbon atoms on the phthiocerol moiety, and n and p on the mycocerosate moieties. (*B*) MALDI-TOF mass spectra of purified DIM and of the membrane fraction of macrophages treated with DIM. (*C*) MALDI-TOF mass spectra of WT Mtb (HR37v) and of the membrane fraction of macrophages infected by H37Rv or by the H37RvΔ*lppX* mutant. M, low intensity peak corresponding to the detection of the matrix molecule in the DIM region of interest. The asterisk highlights the mass of the DIM molecule chosen for the modeling, with m = 18, n = 17, and p = 4.

whether DIM added to host cells is incorporated into their membranes. Human macrophage (THP-1) cells were treated with purified DIM, and the mass spectrum of the extracted lipids was compared with the spectrum of purified DIM. The structure of DIM consists of a long chain of phthiocerol (3-methoxy, 4-methyl, 9,11-dihydroxy glycol) esterified with 2 mycocerosic acids (long-chain multiple methyl-branched fatty acids) (Fig. 1*A*). In agreement with the MycoMass database (16), the purified DIM mass spectrum is characterized by a cluster of pseudomolecular ions $[M + Na]^+$ between m/z = 1,305 and m/z = 1,501 in increments of m/z = 14 (Fig. 1*B*), reflecting the variability of chain lengths and methylations of the molecule. We observed that the spectrum of the extracted lipids from DIM-treated THP-1 cells showed a very similar series of peaks to that of purified DIM (Fig. 1*B*). These peaks were absent in the spectrum of lipid extracts from untreated cells (*SI Appendix*, Fig. S1*A*). Hence, exogenously delivered DIM can be inserted into macrophage membranes and were detectable by MALDI-TOF mass spectrometry.

We next investigated if DIM could be transferred from the *Mtb* envelope to macrophage membranes during infection. To test this, we infected THP-1 macrophages with the wild-type (WT) *Mtb* strain H37Rv for 2 h at a multiplicity of infection (MOI) of 15:1. At 40 h postinfection, the membrane fraction of the infected macrophages showed a mass spectrum similar to the lipid signature of DIM isolated from the H37Rv inoculum (Fig. 1*C*). We noticed a distinct shift toward longer DIM chain lengths, consistent with the reported increase in molecular mass of DIM during *Mtb* infection (17). The residual bacterial contamination of the macrophage membrane fractions was less than 1,500 colony-forming units (cfu), well below the threshold for detection of DIM extracted directly from bacteria (between 10^5 and 10^7 cfu) (*SI Appendix*, Fig. S1*B*). Our data therefore strongly support the model that DIM is transferred from *Mtb* to the membranes of infected macrophages.

To verify whether DIM exposure at the surface of *Mtb* is required for their transfer to macrophage membranes, we infected macrophages with a mutant strain (H37RvΔ*lppX*) lacking LppX, a lipoprotein required for the translocation of DIM to the outer membrane of *Mtb* (18). After infection, we did not observe the typical mass spectrum of DIM in the membrane fraction of H37RvΔ*lppX*-infected cells (Fig. 1*C*). We verified that the WT and mutant strains produced similar amounts of DIM (*SI Appendix*, Fig. S1*C*).

Taken together, these results demonstrate that DIM molecules are indeed transferred to the membranes of macrophages during infection, provided they are exposed at the surface of *M. tuberculosis*.

DIMs Accommodate into a Bilayer Membrane by Adopting a Conical Shape. Given their long aliphatic chains and their overall hydrophobic properties, we sought to understand how DIM might physically be accommodated in a bilayer membrane. We used a multiscale modeling approach to gain insight into the conformation of such a complex lipid embedded in a simple phospholipid bilayer.

During macrophage infection, *Mtb* produces DIM of higher molecular weight than under noninfectious conditions (17) (Fig. 1*C*). We therefore modeled the structure of a DIM molecule with a molecular mass of 1,436 Da (corresponding to a peak of m/z = 1,459, see asterisk in Fig. 1*C*): i.e., having chain lengths and number of methylations corresponding to m = 18, n = 17,

Downloaded at UNIVERSITAT MUENCHEN Bibliothek Bereich Physiologie on November 24, 2019

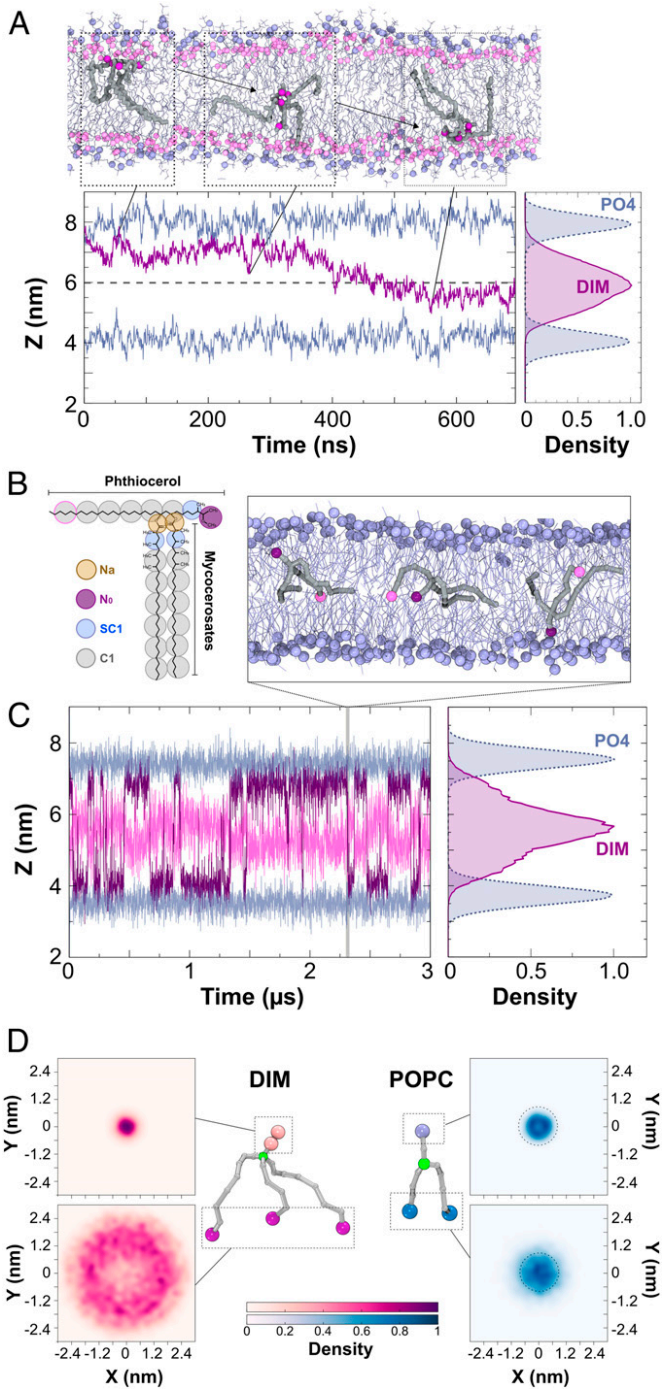

Fig. 2. Position and shape of a single DIM molecule in a POPC bilayer. (*A*, *Top Inset*) Atomistic simulation of a DIM molecule (in gray licorice) showing its passage from one leaflet of the POPC bilayer to the opposite one. DIM oxygen atoms are represented in purple, POPC phosphorous atoms are displayed in light blue, and POPC oxygen atoms in pink. (*A*, *Bottom Left*) In purple, evolution of the z-position for the center of mass of DIM's oxygen atoms during the course of the atomistic simulation. In light blue, averaged z-position of the phosphorous atoms of the POPC molecules. (*A*, *Bottom Right*) Densities of the positions of the DIM lipid and POPC phosphate groups revealing the embedded DIM position in the bilayer. (*B*) Coarse-grained model of the DIM molecule (see *Materials and Methods* and *SI Appendix*, Fig. S3 for details). (*C*) Evolution of N0 and the last C1 particles on the phthiocerol moieties (in purple and pink, respectively) during the course of the CG simulation. This plot shows a C1 particle confined around the interleaflet space while the N0 particle stayed in the proximity of the POPC oxygen atoms. (*Top Inset*) DIM (in gray) transit from one leaflet to the other during CG simulation. (*Right Inset*) Densities of the DIM lipid and POPC phosphate groups. (*D*) The 2D density projections of each extremity for DIM and POPC molecules in the *x*–*y* membrane plane (CG simulation) (see also *SI Appendix*, Fig. S5 displaying densities for atomistic simulations), highlighting the conical shape of DIM and the cylindrical shape of POPC, respectively. Particles depicted in green were used for molecule centering.

and p = 4 (Fig. 1*A*). Then, 800 ns of atomistic molecular dynamics (MD) simulations of a single DIM molecule in a 1-palmitoyl-2-oleoyl-*sn*-glycero-3-phosphocholine (POPC) lipid bilayer revealed that DIM is deeply embedded in the membrane and may transit between the 2 opposing leaflets (Fig. 2*A*). DIM oxygen atoms preferentially remained in the proximity of the POPC ester bonds while the acyl chains stretched into the membrane hydrophobic core. The very long acyl chains (containing up to 27 carbon atoms) prevented confinement of the DIM molecule to 1 single leaflet. Instead, DIM seemed to be accommodated within the phospholipid bilayer by extending these chains in the interleaflets space (see density profile in Fig. 2*A*).

To further explore the dynamics of the DIM molecule within the membrane, we designed a coarse-grained (CG) model (Fig. 2*B*) based on the MARTINI force field (*Materials and Methods* and *SI Appendix*, Fig. S3). This force field is well adapted to model a large variety of lipids and their actions on membranes and proteins (19, 20). CG modeling of a single DIM molecule in a POPC bilayer confirmed that DIM extended its long acyl chains in between the 2 leaflets as seen in the atomistic simulation (Fig. 2 *B* and *C*). Using CG modeling, we were able to extend the simulation to longer time scales to see multiple DIM translocations from one leaflet to the other (Fig. 2*C*). We then increased the number of DIM molecules up to a molar DIM-to-POPC ratio of about 7% (*SI Appendix*, Fig. S4). At low concentrations (1%, 2%, and ~4%), DIM molecules diffused freely inside the bilayer while, at 7%, they started to strongly interact with each other and form aggregates in between the 2 leaflets. This behavior is also observed, both experimentally and computationally, for molecules with similar structural features, like triglycerides (21, 22).

We next sought to understand how the position of the DIM acyl chains in the interleaflet space affected its overall shape. To do so, we projected the positions of the lipid extremities onto the two-dimensional (2D) membrane plane (Fig. 2*D*). When centering the molecule on the junction of the chains, this revealed very large movements of the 3 acyl chain extremities while the most polar end of the phthiocerol chain remained largely static. For POPC, a similar projection displayed a completely different behavior, with comparable densities for both the headgroup and the hydrophobic acyl chain extremities (Fig. 2*D*). Comparable results were obtained from atomistic simulations (*SI Appendix*, Fig. S5). These results can be related to the effective shape of each molecule: while it is known that POPC has a cylindrical shape, consistent with our simulations, which is suitable to form planar lipid membranes, our results indicated that DIM molecules adopt a strongly conical shape in a lipid bilayer.

DIMs Drive the Formation of Nonbilayer Membrane Structures in a DOPE/SOPC Lipid Mixture. This conical molecular shape of DIM may have important consequences for the organization of DIM-containing membranes. Indeed, conical lipids are known to destabilize the lamellar membrane phase (L_α) and favor the appearance of a nonbilayer inverted-hexagonal phase (H_{II}) (23). The transition from an L_α phase to an H_{II} phase can be studied using ^{31}P-NMR spectroscopy by monitoring the NMR spectra at increasing temperature (*Materials and Methods*). We have employed magic angle spinning (MAS) NMR spectroscopy for enhanced sensitivity. A mixture of the phospholipids 1,2-dioleoyl-*sn*-glycero-3-phosphoethanolamine (DOPE) and 1-stearoyl-2-oleoyl-*sn*-glycero-3-phosphocholine (SOPC) (24) has been used for a range of lipids

Downloaded at UNIVERSITAT MUENCHEN Bibliothek Bereich Physiologie on November 24, 2019

to study their propensity to induce nonbilayer phases (25, 26). To study the influence of DIM, we used lipid membranes made of a 3:1 (mol/mol) mixture of DOPE and SOPC (*Materials and Methods*). With this lipid composition, the membranes remained in the L_α phase for temperatures up to 322 K (Fig. 3 *A* and *C*). However, incorporating 5% of DIM into the lipid mixture destabilized the L_α phase and induced a transition from an L_α phase at low temperature (284 K) (Fig. 3*A*) to an H_{II} phase configuration at high temperature (310 K and 322 K) (Fig. 3*A*), as evidenced by the ^{31}P-NMR spectra. Thus, DIMs destabilize the L_α phase in our model membranes and promote the transition to the H_{II} phase.

As a complementary approach to monitor the ability of DIM to induce nonbilayer phases, we performed CG-MD simulations. This method is especially well suited to study lipid phase transitions in lipids (27, 28) and polymers (29, 30). We modeled a stack of 4 lipid bilayers of identical composition (3:1 DOPE/SOPC) as in the ^{31}P-NMR experiments, for temperatures ranging from 280 K to 350 K (see *Materials and Methods* for details). Similar to the ^{31}P-NMR experiments, the membranes remained in the lamellar phase in the absence of DIM (*SI Appendix*, Fig. S6), but a temperature-driven transition occurred when 5% of DIMs were added (Fig. 3*B*). These simulations allow a deeper understanding of the molecular process of the H_{II} phase transition in the presence of DIM. At low temperatures, molecules of DIM formed aggregates in the interleaflet space (Figs. 3*B*, 280 K), as also seen in the POPC bilayer (*SI Appendix*, Fig. S4). Increasing the temperature led to the formation of fusion stalks, hourglass-shaped lipid structures formed between neighboring bilayers. DIM aggregated in these stalks to extend their large hydrophobic tails (Movie S1). This aggregation stabilized and helped to increase the width of the stalks, eventually leading to the formation of tubular water-filled membrane structures (Fig. 3*B*, 310 K). At still higher temperatures (320 K and higher), DIM molecules diffused freely in the hydrophobic membrane core, thus stabilizing the H_{II} configuration (Fig. 3*B*, 320 K and Movie S1).

We deconvoluted the ^{31}P-NMR spectra recorded between 282 K and 322 K in 2 K steps for DOPE/SOPC (3:1) with 5% of DIM, using a set of parameters obtained from reference datasets (*Materials and Methods* and *SI Appendix*, Table S2). The ^{31}P chemical shifts of DOPE and SOPC are different. Therefore, each spinning sideband in our spectra consisted of 2 resolved peaks (Fig. 3*A*), enabling us, in a single spectrum, to independently analyze the percentages of the L_α and H_{II} phases for DOPE and for SOPC. For both lipids, we observed a continuous transition from the L_α to the H_{II} phase described by a sigmoid (Fig. 3*C* and *SI Appendix*, Table S3 and *Supplementary Text*). The phase transition midpoint temperatures (T_{50}) were 303.5 K (± 0.4) for DOPE and 305.3 K (± 0.5) for SOPC. It should be noted that the phase transitions of SOPC and DOPE molecules are not independent from each other. The small difference of 2 °C which is observed reflects the tendency of DOPE molecules to accumulate in nonlamellar domains more than SOPC molecules, a tendency observed in most of the tested conditions (*SI Appendix*, Table S3). This result is in agreement with previous studies showing that conical DOPE prefers the H_{II} phase, in contrast to cylindrical POPC lipids (31), and may also be related to the sorting of lipids as a function of the curvature (32, 33). In the CG-MD simulations, we evaluated the percentage of L_α phase as a function of temperature from the distribution of lipid tilt angles

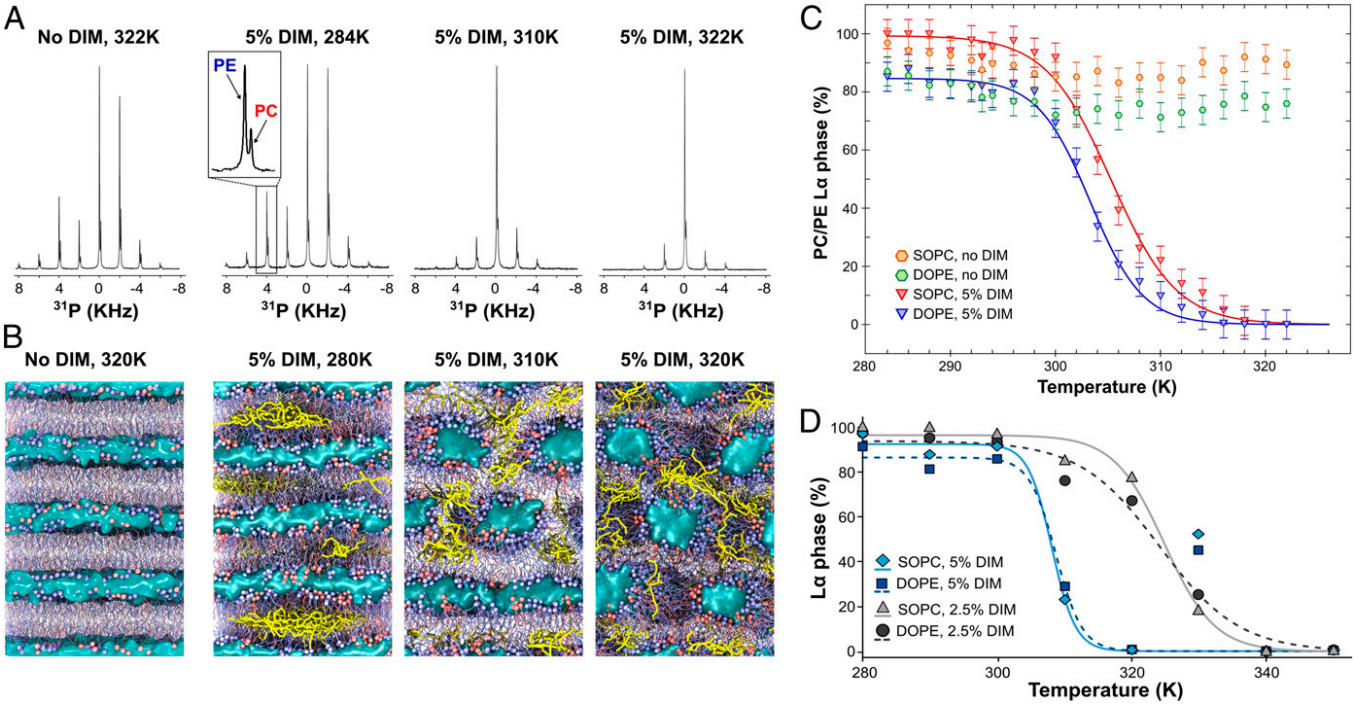

Fig. 3. DIMs induce H_{II} phases for a DOPE/SOPC (3:1, mol/mol) lipid mixture. (*A*) ^{31}P-NMR spectra at different temperatures for DOPE/SOPC (3:1, mol/mol) without DIM or containing 5% of DIM. In the MAS ^{31}P-NMR spectra, each spinning sideband consists of a DOPE and an SOPC peak. (*B*) Coarse-grained models of the phase transition in DOPE/SOPC (3:1, mol/mol) without DIM or containing 5% of DIM. Increasing the temperature leads to the formation of tubular structures for the DIM-containing systems while the systems without DIM stay fully lamellar. Snapshots shown are taken at the end of the 3-μs simulations. SOPC molecules are colored in red. DOPE molecules are colored in blue. DIM molecules are colored in yellow. Water molecules are represented as a blue surface. (*C*) Spectral deconvolution of the ^{31}P-NMR spectra giving the percentage of the L_α phase as a function of the temperature for DOPE/SOPC (3:1) without DIM (orange and green hexagons) and with addition of 5% DIM (red and blue triangles). In the case of 5% DIM, the phase transition can be approximated by a sigmoid (red and blue lines). (*D*) SOPC and DOPE phase transitions calculated from CG-MD simulations for 2.5% and 5% of DIM. For the DOPE/SOPC mixture with 5% of DIM, we removed the outlier values at 330 K from the curve fitting based on statistical tests (*SI Appendix*, *Supplementary Text*).

Downloaded at UNIVERSITAT MUENCHEN Bibliothek Bereich Physiologie on November 24, 2019

(*SI Appendix*, *Supplementary Material*), for SOPC and DOPE (Fig. 3*D*). Here, too, we observed continuous phase transitions that were fitted by a sigmoid, with a midpoint transition temperature of ~308 K (*SI Appendix*, Table S3), which is in broad agreement with the ^{31}P-NMR experiments.

CG-MD simulations revealed that the first stage of the mechanism through which DIMs drive the L_α-to-H_{II} phase transition involves their aggregation in membrane stalks. Hence, blocking the formation of stalks would be expected to reduce the effect of DIM. To test this, and validate our hypothesis, we replaced a fraction of SOPC with lysophosphatidylcholine (lysoPC), a lipid known to hinder the formation of fusion stalks (34, 35). ^{31}P-NMR experiments on liposomes of DOPE/SOPC/lysoPC (75:25:0), (75:20:5), and (75:15:10), each containing 2.5% of DIM, revealed an increase of the transition midpoint temperature T_{50} (*SI Appendix*, Fig. S8) with increasing percentage of lysoPC, highlighting a diminished effect of DIM when fusion stalk formation is inhibited. We next performed CG-MD simulations to understand the molecular process involved. Consistent with the NMR experiment, including lysoPC in the simulation increased the value of T_{50} (*SI Appendix*, Fig. S8*A*). From these simulations, we observed that the effect of lysoPC did not involve a direct interaction with DIM as lysoPC was spread throughout the membranes (*SI Appendix*, Fig. S8*B*). Indeed, ^{31}P-NMR experiments on DOPE/SOPC (5:1, mol/mol), which displays an L_α-to-H_{II} transition without DIM, also showed an increase in T_{50} upon replacing a fraction of SOPC by lysoPC (*SI Appendix*, Fig. S7). Thus, limiting the formation of stalks decreased the ability of DIM to effectively drive the formation of nonbilayer membrane structures.

Effects of DIM on More Complex Lipid Mixtures. The DOPE/SOPC (3:1, mol/mol) mixture can easily be driven toward the inverted hexagonal phase by the inclusion of extraneous conical lipids. To study the action of DIM lipids in more natural, curvature-neutral systems, we also examined 2 different lipid mixtures. First, we performed ^{31}P-NMR experiments on liposomes of 1-palmitoyl-2-oleoyl-glycero-3-phosphocoline (POPC)/palmitoyl-2-oleoyl-*sn*-glycero-3-phosphoethanolamine (POPE)/cholesterol/sphingomyelin (molar ratio 4:3:2:1), a composition chosen to approach the macrophage membrane (36). In the range of temperatures tested (284 K to 324 K), we did not observe a transition to the H_{II} phase for this mixture, neither without DIM nor with the incorporation of 2.5% of DIM lipids (*SI Appendix*, Fig. S9*A*). Interestingly, CG-MD simulations predicted that, even with 5% of DIM lipids, a full H_{II} transition would only be reached at very high temperatures (370 K and above) (*SI Appendix*, Fig. S9*B*). We then examined a mixture of POPE/cholesterol/sphingomyelin (molar ratio 7:2:1). This system was expected to remain lamellar over the range of temperatures studied (284 K to 324 K) as the full H_{II} transition of POPE, the major constituent of this mixture, is only reached at ~350 K (37). Indeed, ^{31}P-NMR spectra revealed only a lamellar phase configuration without DIM (*SI Appendix*, Fig. S10*A*). However, the inclusion of 5% of DIM in this system drove an L_α-to-H_{II} transition in between 310 K and 324 K (*SI Appendix*, Fig. S10*B*), with a midpoint temperature at 318 K (± 0.16). CG-MD simulations also showed a transition between 310 K and 320 K with the addition of 5% of DIM lipids while the lipid mixture without DIM lipids remained in a fully lamellar state for this range of temperatures (*SI Appendix*, Fig. S10*C*).

By analyzing CG-MD simulations, we examined how the addition of DIM lipids may change the biophysical properties of lamellar systems. To this end, we first calculated the membrane lateral pressure of the POPC bilayer with different concentrations of DIM (*SI Appendix*, Fig. S4*B*). Increasing the concentration of DIM lipids changed the pressure profile of the system. The change in pressure in the center of the bilayer highlights the positioning of DIM lipids in between the 2 leaflets. This may help lower packing stress for other conical lipids, such as phosphoethanolamine (PE) lipids, which may in turn decrease the energy barriers for hexagonal phase formation. Thus, DIM lipids may create a spatially inhomogeneous distribution of the different lipids. To test this hypothesis, we performed CG-MD simulations of a 28 × 28-nm^2 membrane patch composed of a mixture of POPC/POPE/cholesterol/sphingomyelin (molar ratio 4:3:2:1) with the addition of 2.5% or 5% of DIM lipids. For both concentrations, we observed an enrichment of POPE around the DIM aggregates (Fig. 4).

Altogether, the combination of ^{31}P-NMR and CG-MD simulations revealed the ability of DIM lipids to perturb membrane organization and promote a phase transition from the lamellar to the inverted hexagonal phase. The molecular mechanism involves an initial aggregation of DIM lipids which then can drive the formation and the stabilization of fusion stalks, leading, in some cases, to a complete destabilization of the lamellar phase in favor of the inverted hexagonal phase.

High Potency of DIM to Induce Nonbilayer Phase in Comparison to Other Lipids. We compared the ability (potency) of DIM to induce the H_{II} phase for a DOPE/SOPC (3:1, mol/mol) mixture to that of lipids with different structural features using ^{31}P-NMR. We first tested the effect of the concentration of DIM on the formation of the H_{II} phase. Fig. 5*B* shows that decreasing the DIM concentration to 2.5% and 1% still led to the formation of the full H_{II} phase, albeit at a higher temperature. The increased transition midpoint temperature (Fig. 5*B*) reveals a dose–response relationship, which is also observed in CG-MD simulations Fig. 3*D*). We then tested the effect of the triglyceride tripalmitin (Fig. 5*A*), which, like DIM, has 3 acyl chains. However, incorporation of either 2.5% or 5% of tripalmitin did not induce a full H_{II} phase

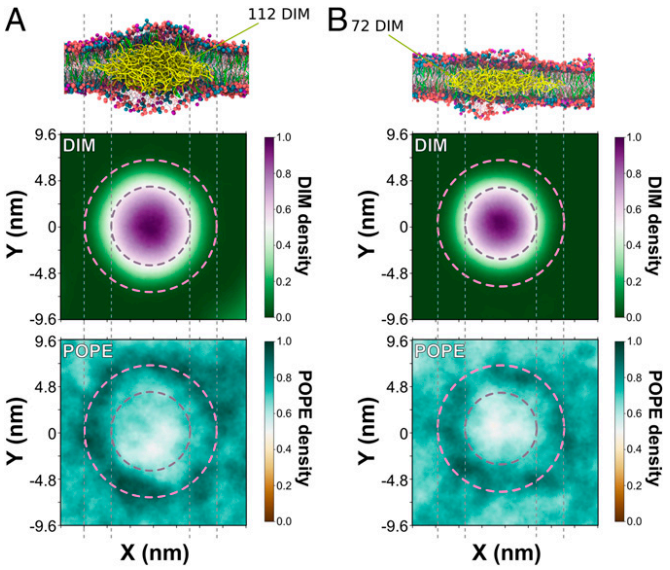

Fig. 4. DIM aggregate in a POPC-POPE-cholesterol-sphingomyelin lipid mixture. Simulations of a 28 × 28-nm^2 patch of a macrophage-like membrane constituted of POPC/POPE/cholesterol/sphingomyelin (ratio 4:3:2:1) at 310 K with 5% of DIM (*A*) or 2.5% of DIM (*B*). For each system, at the end of 10 μs of simulations, 1 or several aggregates were formed in the center of the bilayer. Here, we focus on the largest aggregate. (*Top* illustration) DIM aggregates after 10 μs of simulation. POPC molecules are colored in red. POPE molecules are colored in blue. Cholesterol molecules are colored in green. Sphingomyelin molecules are colored in purple. DIM molecules are colored in yellow. (*Second* and *Third* row) The density profile for both leaflets (top view of the membrane) of DIM and POPE lipids obtained by centering the DIM aggregates for the last 2.5 μs. Dashed lines broadly define the periphery of DIM aggregates where POPE lipids tend to be enriched while they seem to be depleted in the center of the aggregate.

Downloaded at UNIVERSITAT MUENCHEN Bibliothek Bereich Physiologie on November 24, 2019

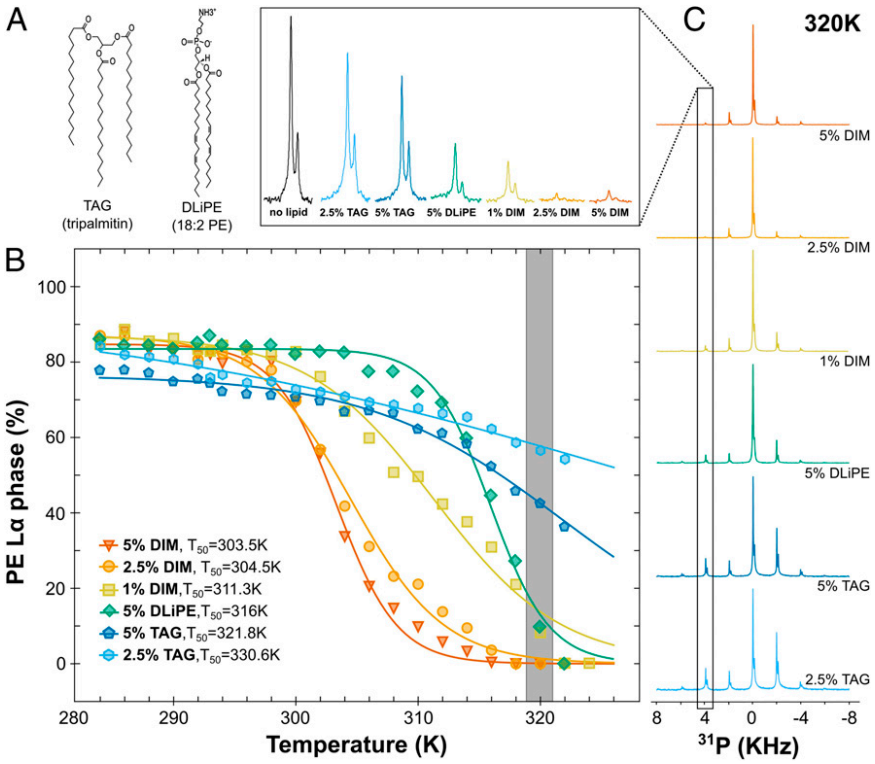

Fig. 5. Comparison of DIM potency to induce nonbilayer phase with lipids of different shapes. (*A*) Molecular structures of the triacylglycerol (TAG) tripalmitin and of 1,2-dilinoleoyl-*sn*-glycero-3-phosphoethanolamine (DLiPE). (*B*) Evolution of the L_α-to-H_{II} phase transition for the DOPE molecules as a function of temperature for DOPE/SOPC (3:1) containing different concentrations of DIM, DLiPE, and TAG (see also *SI Appendix*, Fig. S11 for the respective curves for SOPC molecules). For clarity, error bars are omitted. As seen in Fig. 3, the error was evaluated to ±5%. The gray bar represents the points obtained from the spectra highlighted in *C*. (*C*) ^{31}P-NMR spectra for the lipid mixtures containing TAG, DLiPE, or DIM at 320 K. The second rotation band (4 kHz), which is strongly related to the evolution of the L_α phase, is magnified in the *Top*. For comparison, the black peak depicts the second rotation band of DOPE/SOPC (3:1) at 320 K.

transition (Fig. 5*B*). Thus, the effect of DIM on nonbilayer structure formation did not seem to be uniquely related to its 3-legged structure.

We finally analyzed the ability of 1,2-dilinoleoyl-*sn*-glycero-3-phosphoethanolamine (DLiPE) to induce the L_α-to-H_{II} phase transition and compared it with DIM. With 2 double bonds in each acyl chain (Fig. 5*A*), DLiPE is expected to be a strong enhancer of hexagonal phase formation (38). With 5% of DLiPE, we observed a full H_{II} phase transition already at 322 K (Fig. 5 *B* and *C*) and a transition midpoint temperature for DOPE of 316 K (± 0.4). However, this value is higher than for 5% DIM (303.5K ± 0.4), 2.5% DIM (304.5K ± 0.5), and even 1% DIM (311.3K ± 1.0) (*SI Appendix*, Table S3). Thus, DIM molecules are strong inducers of nonbilayer phases, even at low concentrations.

Lipid shape can be assessed by studying inverted hexagonal phase in different lipid mixtures (38). Here, using the L_α-to-H_{II} phase transition temperature as a measure to assess lipid conical shape, we ranked the shape of the different molecules: DIMs were strongly conical and DLiPEs were less conical, while the tripalmitins were the least conical.

Lipid Shape Modulates the Entry of *Mtb* and Zymosan Particles into Macrophages. In our previous experiments, the DIM-deficient mutant H37Rv*ΔppsE* appeared to infect macrophages with a lower efficiency than the WT strain. Coating these DIM-deficient mutant bacteria with DIM restored the WT phenotype while coating mutants with tripalmitin did not have an effect (8). These results may now be related to their respective conical shapes: strongly conical for DIM and less conical for tripalmitin. To test whether it is specifically the conical shape of DIM that helps *Mtb* to invade macrophages, we evaluated the impact of exogenously added DIM and various other lipids on the capacity of this mutant to invade human monocyte-derived macrophages (hMDM) in comparison to the WT H37Rv strain (Fig. 6*A*). We confirmed that the DIM-deficient mutant infected a lower percentage of macrophages than the WT strain (Fig. 6 *B* and *C*). Pretreatment of macrophages with DIM restored the percentage of infected cells to a level comparable to that observed with the WT H37Rv strain in untreated macrophages (Fig. 6 *B* and *C*). Notably, treating macrophages with the conical phospholipid POPE also enhanced the percentage of macrophages infected with the H37Rv*ΔppsE* mutant whereas treatment with the cylindrical lipid POPC had no significant effect (Fig. 6*C*). These data support the hypothesis that the conical shape of DIM, which induces nonbilayer membrane structures, increases the efficiency of *Mtb* to infect macrophages.

To determine whether this effect of DIM on macrophages is restricted to infection by *Mtb*, we examined the effect of DIM and other lipids on the uptake of zymosan (Fig. 6*D*) a fungal polysaccharide frequently used to study nonopsonic phagocytosis (39). We found that macrophage preincubation with DIM also increased zymosan uptake by macrophages in comparison to untreated conditions, as did preincubation with POPE but not with POPC (Fig. 6*E*). These data indicate that DIM and other conical lipids generally promote phagocytosis by macrophages.

Discussion

While lipid transfer from *Mtb* to the macrophage membranes during infection had been demonstrated for glycolipids (40), this was never shown for DIM. By using MALDI-TOF mass spectrometry, we established that DIM molecules exposed at the envelope of *Mtb* are indeed transferred to the macrophage

Downloaded at UNIVERSITAT MUENCHEN Bibliothek Bereich Physiologie on November 24, 2019

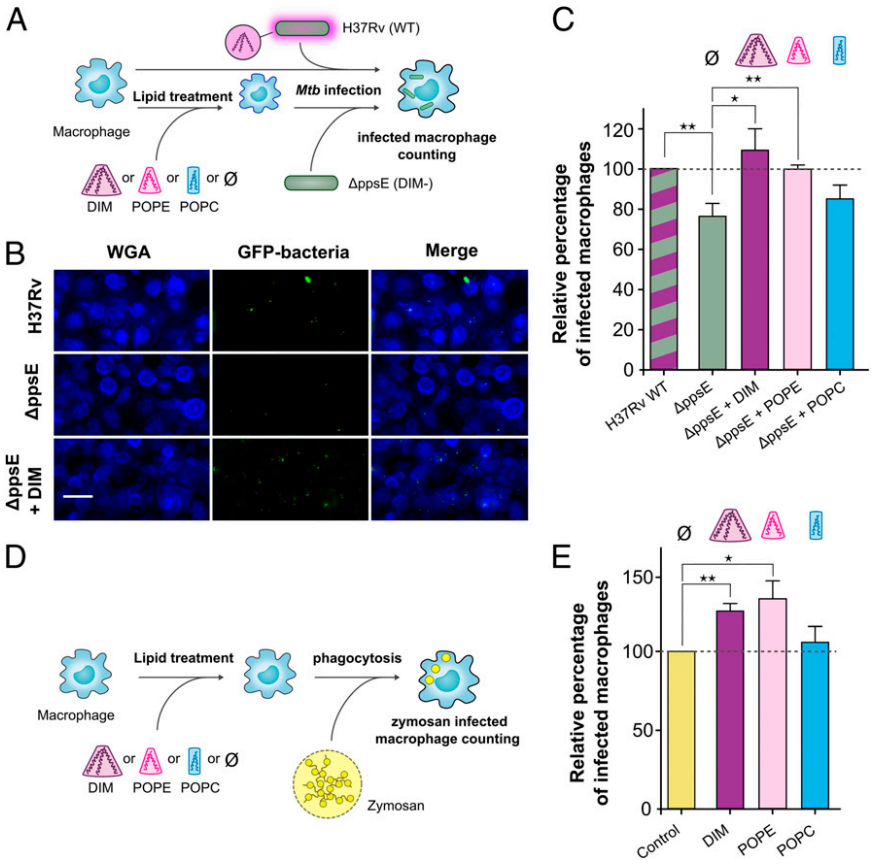

Fig. 6. Lipid shapes modulate the entry of the MtbΔ*ppsE* mutant and zymosan into macrophages. (*A*) Macrophages were incubated at 37 °C for 1 h with lipid solvent (Ø) or 70 μM lipids (DIM, POPC, and POPE) and subsequently exposed to GFP-expressing H37Rv WT or ΔppsE (MOI 10:1) for 1 h. Cells were then fixed and processed for the quantification of infected macrophages by fluorescence microscopy. (*B*) Representative fluorescence microscopy images of untreated or DIM-treated macrophages stained with WGA (membrane marker, blue) and infected with GFP-expressing H37Rv WT or Δ*ppsE* (green). (Scale bar: 30 μm.) (*C*) The histogram represents the percentage of macrophages infected with Δ*ppsE* in lipid-treated and untreated macrophages, expressed with respect to H37Rv WT (100%). (*D*) Macrophages were incubated with solvent (Ø) or lipids and then put in contact for 1 h with zymosan particles (MOI 30:1). (*E*) Percentages of macrophages infected with zymosan in untreated cells or cells treated with lipids. Values are expressed with respect to the uptake of zymosan in untreated cells (100%). The values are means ± SEM of 8 to 10 separate experiments. The significance of difference in the percentage of macrophage infection between H37Rv WT and Δ*ppsE* or between untreated and lipid-treated cells was evaluated: $*P < 0.05$; $**P < 0.015$.

membranes during infection (Fig. 1). We envision 2 mechanisms that could account for this process. DIM may be exchanged by direct contact between the surface of the bacteria and the macrophage membrane at contact sites. Such direct exchange of cholesterol and cholesterol-glycolipids has been observed between *Borrelia burgdorferi* and HeLa cells (41). Alternatively, DIM could be transported in the membranes of extracellular vesicles, which are known to be excreted by *Mtb* and other mycobacteria (42), followed by fusion of these vesicles with the plasma membrane of the macrophages. Lipid exchange mediated by vesicle fusion was shown for *B. burgdorferi* (41) and for *Pseudomonas aeruginosa* (43). For the latter process, lipid transfer could be favored by the conical shape, which promotes the fusion of vesicles with the host cell membrane (44). Here, by combining ^{31}P-NMR with MD simulations, we demonstrated that DIM can adopt such a conical shape and promote the formation of nonbilayer (inverted hexagonal) membrane phases (Fig. 3), structures important for efficient membrane fusion (45). Membrane fusion may also be important for sealing of the phagosomal membrane during the ultimate stage of phagocytosis. Notably, our results showed that even DLiPE, a strong enhancer of nonbilayer phases, did not match the strength of DIM in promoting nonbilayer structures (Fig. 5). This may be explained by the fact that DIM lipids preferentially aggregate in transient stalks (Fig. 3*B* and Movie S1) to stabilize them, thereby enhancing nonbilayer phase formation. This shape may also be adopted by other long acyl chain lipids that are important for *Mtb* infection (2) and are transferred to the host cell membrane (40), such as trehalose mono- and di-mycolate and the phenolic glycolipids, molecules structurally related to DIM. While the conical shape is common to PE and DIM lipids, we highlight an additional distinctive property of DIM lipids. The highly hydrophobic nature of DIM may constrain these lipids to aggregate in between the 2 leaflets (as seen in Figs. 3*B* and 4 and *SI Appendix*, Fig. S4*A*). This localization may destabilize the lamellar phase (*SI Appendix*, Fig. S4*B*) as was seen recently for other apolar lipids (46, 47), while favoring the partition of other lipids, such as PEs, (as seen in Fig. 4) that can lower activation energy barriers: e.g., for cell fusion.

There is now ample evidence that lipids can modulate membrane protein structure (48) and functions (49, 50). As seen for lipids such as diacylglycerol (51), the conical shape of DIM may modulate membrane protein activity. Accordingly, we find that DIMs increase the nonopsonic phagocytosis of zymosan, a process well known to be mediated by a repertoire of membrane receptors, including complement receptor 3 (CR3) (39) and the mannose receptor (52). DIM may act on membrane proteins via different biophysical mechanisms. First, DIM may impose curvature on the host membrane (12), which in turn may modulate integral membrane protein sorting (53, 54) and function (55). DIM could also trigger reorganization of lipid nano-domains to

Downloaded at UNIVERSITAT MUENCHEN Bibliothek Bereich Physiologie on November 24, 2019

modulate signaling platforms (14, 56). Thus, our findings should open avenues for understanding how *Mtb* subverts other receptors involved in its recognition by the immune system (57), including Toll-like receptors, NOD-like receptors, and C-type lectin receptors.

Modulating the activity of membrane proteins will ultimately modulate cellular functions. Indeed, we showed that DIMs promote *Mtb* infection (Fig. 6). To confirm the relevance of the conical shape, we showed that conical POPE lipids, but not cylindrical POPC lipids, added to macrophages also restored the infection capacity of a DIM-deficient *Mtb* mutant and improved phagocytosis (Fig. 6). Our results also shed light on previous observations showing that a DIM-deficient *Mtb* mutant coated with tripalmitin lipid was less effective in infecting macrophages than DIM-coated mutants (8). This can now be understood by the fact that tripalmitin did not promote formation of a nonbilayer phase transition in our model membranes (Fig. 5) and hence did not display a strong conical shape. Our results demonstrate that the conical shape of a lipid promotes phagocytosis. The effect of the conical shape of DIM on disorganizing the membrane may also play a role in the induction of phagosomal membrane rupture and cell death (58, 59). Altogether, understanding how the molecular shape of DIM lipids and their biophysical properties affect biological membranes may help to design host-directed therapeutic strategies to fight tuberculosis (60), by preventing the infection of macrophages by *Mtb*.

Materials and Methods

Antibodies, Lipids, and Reagents. The rabbit polyclonal antibody against mycobacteria was produced as previously described (8). The Rhodamine Red-conjugated goat anti-rabbit secondary antibody and wheat germ agglutinin (WGA), Alexa Fluor 350 conjugate were purchased from Invitrogen. DIMs were extracted from *Mycobacterium canetti* (*SI Appendix, Supplementary Materials and Methods*). 1-palmitoyl-2-oleoyl-*sn*-glycero-3-phosphocholine (16:0-18:1 PC, POPC), 1-palmitoyl-2-oleoyl-*sn*-glycero-3-phosphoethanolamine (16:0-18:1 PE, POPE), 1-stearoyl-2-oleoyl-*sn*-glycero-3-phosphocholine (18:0-18:1 PC, SOPC), 1,2-dioleoyl-*sn*-glycero-3-phosphoethanolamine (18:1-18:1 PE, DOPE), 1-palmitoyl-2-hydroxy-*sn*-glycero-3-phosphocholine (16:0 lysoPC), 1,2-dilinoleoyl-*sn*-glycero-3-phosphoethanolamine (18:2 PE, DLiPE), cholesterol, and egg sphingomyelin were purchased from Avanti Polar Lipids (Alabaster, AL). Tripalmitin was purchased from Sigma-Aldrich. The other reagents were purchased from Sigma-Aldrich, except when specifically mentioned.

NMR Data Acquisition. Phosphorus NMR spectra were acquired on a 500-MHz Bruker Avance spectrometer, in an HRMAS probe, with deuterium lock. The lipid samples [typically 6 mg of total lipids in 50 μL of Tris buffer (10 mM Tris, 1 mM EDTA, pH 7.4)] were inserted into 4-mm rotors with spherical inserts. The temperature of the sample could be varied between 278 K and 324 K and was controlled to ± 0.1 K with a Bruker variable temperature unit. The temperature was calibrated using the known temperature dependence of methanol chemical shifts. ^{31}P chemical shift anisotropies (CSAs) were determined from the spinning sideband manifolds at a spinning frequency of 2,000 ± 1 Hz. MAS spectra were obtained with a spin-echo sequence ($\pi/2$-τ-π) where the $\pi/2$ pulse had a length of 5.3 μs (at a power of 107 W), applied at the lipids' isotropic resonance frequency, and the interpulse delay, τ, was 20 μs. The dwell time was 1 μs, the acquisition time 65 ms, the relaxation delay 1 s, and the number of scans 4,096. No proton decoupling was applied during acquisition since it was shown to have no effect on the linewidth at a 2-kHz spinning frequency (i.e., well above the ^{1}H-^{31}P dipolar coupling of ∼500 Hz in fluid lipid bilayers). For every sample, a ^{1}H NMR spectrum at a spinning frequency of 10 kHz was acquired in order to calibrate the ^{1}H (using the methylene peak at 1.25 parts per million [ppm] with respect to TMS) and ^{31}P chemical shifts (with respect to phosphoric acid at 0 ppm, using $\gamma_P/\gamma_H = 0.40480742$). The observed ^{31}P isotropic chemicals shifts were −1.00 ± 0.02 ppm for the phosphatidylcholine head group (in SOPC) and −0.27 ± 0.02 ppm for the phosphatidylethanolamine head group (in DOPE) and varied only slightly with the lipid compositions explored. Typical linewidths were 40 to 60 Hz (i.e., ∼0.25 ppm) so that the PC and PE sideband patterns were well resolved and could be fitted independently.

Every liposome sample was equilibrated overnight at 277 K before NMR measurements. We then measured its ^{31}P MAS spectrum at temperatures from 284 K to 324 K, in 2 K increments every 100 min (25-min equilibration plus 75-min acquisition time for each temperature). For lipid mixtures which did not undergo a lamellar to inverse-hexagonal phase transition (i.e., with a small proportion of DOPE), the spectra were shown to be fully reversible when going down from 324 K to 284 K. However, once the H_{II} phase had formed, it did not revert to the lamellar phase, at least after 1 day of equilibration at 284 K. Hence, all measurements were done for increasing temperatures, starting from the lowest temperature, taking care of maintaining the liposomes at low temperature during their preparation and before NMR measurements. The actual insertion yield of DIM in the lipid bilayers was determined by ^{1}H-NMR (*SI Appendix, Supplementary Text*).

Spectral Deconvolution. We analyzed each ^{31}P spinning sideband manifold using the solid line shape analysis tool (SOLA) available in Topspin 3.5. CSA parameters were calculated using the Haeberlin convention for the anisotropy values $\Delta\delta = \delta_{//} - \delta_{\perp}$ as commonly done in the membrane literature and as explained before (61). We estimated the uncertainty of $\Delta\delta$ values to be ± 0.2 ppm, based on several measurements and fitting performed on independent samples. We first determined the CSA parameters of lipids organized in a single phase (e.g., SOPC for the lamellar L_α phase and DOPE for the H_{II} phase), at several temperatures between 284 K and 324 K. The CSA parameters for each lipid and each phase varied slightly and linearly with temperature, due to increased motion at higher temperatures: from 49.6 ± 0.2 ppm (293 K) to 45.0 ± 0.2 ppm (333 K) for SOPC in the L_α phase; and from −22.2 ± 0.2 ppm (278 K) to −20.1 ± 0.2 ppm (333 K) for DOPE in the H_{II} phase. The following linear regressions were obtained: $\Delta\delta = -0.0944\ T + 76.599$ for SOPC in the L_α phase and $\Delta\delta = -0.0409\ T - 33.627$ for DOPE in the H_{II} phase, where T is the temperature in Kelvin; these regressions were used to calculate CSA values at intermediate temperatures. Since the lipids in the H_{II} phase experience additional motional averaging due to lateral diffusion around the aqueous channels, their CSA is obtained by averaging 2 components, $\delta_{//}$ and $\delta_{\perp}$, divided by 2, for reasons discussed by Cullis and De Kruijff (62). The CSA values in the L_α and H_{II} phases have opposite signs. Hence, the CSA value of SOPC in the H_{II} phase was taken to be −0.5 times its value in the L_α phase while the CSA value of DOPE in the L_α phase was 2 times its value in the H_{II} phase. Knowing the temperature-dependent CSA parameters for both lipids in both phases allowed a drastic reduction of the number of parameters to be fitted when analyzing lipid mixtures in which the 2 phases coexist. After optimizing the peak positions and linewidths, the SOLA fitting algorithm only has to search for the L_α-H_{II} proportions that best reproduce the experimental spectra. The intensity of the spinning sideband at +4 kHz is a good reporter of the proportion of L_α phase since this peak is almost absent from the typical H_{II} phase spinning sideband manifold (63) (Fig. 5*C*). This fitting protocol was very robust and prevented the artifacts and instabilities arising from fitting too many parameters. We should stress that our procedure is based on the assumption that the spectra consist of a linear combination of the spectra of the 2 lipids in the L_α and H_{II} phases, possessing CSA parameters identical to their values in the pure phases at the same temperature. This simplifying assumption was sufficient to characterize the lipid phase transitions although we cannot exclude that the actual lipid behavior is more complex.

MD Simulations. The atomistic MD simulations were performed with the Amber16 software (64) (http://ambermd.org) in combination with Lipid14 (65) and general AMBER force field (Gaff) (66). The system contained a membrane of 300 POPC molecules and was solvated with a TIP3P water model using the CHARMM-GUI server (67, 68). The DIM molecule was positioned in the POPC bilayer with the polar core in the proximity of the POPC oxygen atoms (Fig. 2*A*). In order to avoid steric clashes of the DIM molecule with POPC, the system was initially minimized by executing 1,500 iterations of the steepest descent (SD) algorithm, followed by 1,500 iterations of the conjugate gradient (CG) algorithm, with weakly restrained solute (k = 10 kcal/mol/Å^2). Next, a short 100-ps MD run was performed on weakly restrained solute with temperature varying linearly from 0 to 303 K. The temperature control was achieved using the Langevin dynamics with the collision frequency parameter γ equal to 1.0 ps^{-1}. The integration step used in this run was 1 fs. Throughout the calculations, a cutoff of 10 Å was used for electrostatic interactions. The MD simulation continued with the equilibration of the system, consisting of 10 consecutive MD steps of 500 ps each, at constant temperature of 303 K with no restraints, with the integration step of 2 fs. The production run was then launched for 800 ns with constant pressure of 1 bar. The Langevin dynamics was used to control the temperature, with $\gamma = 1.0$ ps^{-1}, while the pressure was controlled by the anisotropic Berendsen barostat with the pressure relaxation time $\tau_p = 1$ ps. Bonds involving hydrogen were constrained with the SHAKE algorithm.

Downloaded at UNIVERSITAT MUENCHEN Bibliothek Bereich Physiologie on November 24, 2019

Coarse-grain simulations were performed using GROMACS 2016 (69) with the MARTINI force field 2.2 (70, 71). We have designed the CG model of DIM by following the original MARTINI parametrization strategy (72). We approximated 3 to 4 heavy atoms constituting the long hydrophobic acyl chains by 1 C1 particle. Small methyl branched parts were approximated by a small particle SC1. The slightly polar extremity of the phthiocerol chain was approximated by an N_0 particle while the glycerol ester moieties were represented by an intermediate hydrophobicity particle Na as usually done for other phospholipids (Fig. 2*B*). Force constants and equilibrium values for bonds and angles were extracted from the atomistic simulation (*SI Appendix*, Fig. S3). All of the systems were first gradually equilibrated as proposed in the CHARMM-GUI MARTINI Maker protocol (73). Coulomb interactions were treated using the reaction-field potential, and Lennard–Jones interactions were treated using shifted potentials with a cutoff radius of 1.1 nm. For planar systems of pure SOPC, DIM/DLiPE molecules embedded in a POPC bilayer, or composed of a mixture of POPC/POPE/cholesterol/sphingomyelin (with and without DIM molecules), pressure was maintained at 1 bar using the Parrinello–Rahman algorithm (74) with a semiisotropic pressure control. The temperature was kept at 310 K using the v-rescale algorithm (75). For pure DOPE, SOPC/DOPE, POPC/POPE/cholesterol/sphingomyelin, and POPE/cholesterol/sphingomyelin systems undergoing lamellar-to-hexagonal transitions, we used the protocol described by Marrink and Mark (27). We stacked 4 membranes with a hydration level of ∼2 to 3 water CG-particles per lipid (equivalent to approximately 9 to 10 atomistic water molecules) in order to see the phase transition in a reasonable amount of time, as detailed by Marrink and Mark (27). A Berendsen thermostat in combination with a Berendsen barostat (76) was used. A fully anisotropic coupling pressure was applied with a reference pressure of 1 bar. Systems were equilibrated at 280 K, and then 8 to 11 different simulations were launched, with temperatures ranging from 280 K to 380 K (depending on the system studied) with an increment of 10 K. In all CG systems, a time step of 20 fs was used. See *SI Appendix*, Table S1 for a summary of the simulations. Parameters for CG and atomistic representations of DIM lipids will be available on the MARTINI website cgmartini.nl and at the address https://github.com/MChavent. Density profiles were performed using the Gromacs tool density (http://manual.gromacs.org/documentation/2016/onlinehelp/gmx-density.html). The lateral pressure profile was calculated using the modified version of Gromacs: Gromacs-LS (http://www.mdstress.org). MD simulation figures were performed using VMD (77). Scripts used to analyze MD simulations are available at https://github.com/MChavent.

Data Availability. MD simulation material and scripts, as well as tables for NMR phase transitions, are available at https://github.com/MChavent/DIM_data.

A detailed description of materials and methods is provided in *SI Appendix, Supplementary Materials and Methods*.

ACKNOWLEDGMENTS. This work was supported by CNRS-Mission pour les Initiatives Transverses et Interdisciplinaires Grants PEPS MPI 2018 and "Modélisation du vivant" 2019, Agence Nationale de la Recherche Grant ANR-16-CE15-0003, the Fondation pour la Recherche Médicale (FRM) ("Equipe FRM" Grant DEQ20160334879), and the Centre National de la Recherche Scientifique (CNRS). J.A. was the recipient of a PhD scholarship from the French government. This work was granted access to the high performance computing resources of the Calcul en Midi Pyrénées supercomputing center under allocation 2019-17036. C.A.-D. thanks the Toulouse Réseau Imagerie-Genotoul Imaging facility (Toulouse, France). M.C. thanks S. J. Marrink for providing setup details for modeling hexagonal phases. We acknowledge Life Science Editors for proofreading the manuscript. We thank Olivier Neyrolles, Jérôme Nigou, Laurence Salomé, and Justin Teissié for fruitful discussions and support.

1. M. Jackson, The mycobacterial cell envelope-lipids. *Cold Spring Harb. Perspect. Med.* **4**, a021105 (2014).
2. M. A. Forrellad *et al*., Virulence factors of the Mycobacterium tuberculosis complex. *Virulence* **4**, 3–66 (2013).
3. J. S. Cox, B. Chen, M. McNeil, W. R. Jacobs, Jr, Complex lipid determines tissue-specific replication of Mycobacterium tuberculosis in mice. *Nature* **402**, 79–83 (1999).
4. T. A. Day *et al*., Mycobacterium tuberculosis strains lacking surface lipid phthiocerol dimycocerosate are susceptible to killing by an early innate host response. *Infect. Immun.* **82**, 5214–5222 (2014).
5. N. C. Howard *et al*., Mycobacterium tuberculosis carrying a rifampicin drug resistance mutation reprograms macrophage metabolism through cell wall lipid changes. *Nat. Microbiol.* **3**, 1099–1108 (2018).
6. A. Arbués, G. C. Lugo-Villarino, O. Neyrolles, C. Guilhot, C. Astarie-Dequeker, Playing hide-and-seek with host macrophages through the use of mycobacterial cell envelope phthiocerol dimycocerosates and phenolic glycolipids. *Front. Cell. Infect. Microbiol.* **4**, 173 (2014).
7. C. J. Cambier *et al*., Mycobacteria manipulate macrophage recruitment through coordinated use of membrane lipids. *Nature* **505**, 218–222 (2014).
8. C. Astarie-Dequeker *et al*., Phthiocerol dimycocerosates of M. tuberculosis participate in macrophage invasion by inducing changes in the organization of plasma membrane lipids. *PLoS Pathog.* **5**, e1000289 (2009).
9. C. Astarie-Dequeker, J. Nigou, C. Passemar, C. Guilhot, The role of mycobacterial lipids in host pathogenesis. *Drug Discov. Today Dis. Mech.* **7**, e33–e41 (2010).
10. M. Nitenberg *et al*., The potent effect of mycolactone on lipid membranes. *PLoS Pathog.* **14**, e1006814 (2018).
11. H. Nakayama *et al*., Lipoarabinomannan binding to lactosylceramide in lipid rafts is essential for the phagocytosis of mycobacteria by human neutrophils. *Sci. Signal.* **9**, ra101 (2016).
12. T. Harayama, H. Riezman, Understanding the diversity of membrane lipid composition. *Nat. Rev. Mol. Cell Biol.* **19**, 281–296 (2018).
13. V. A. Frolov, A. V. Shnyrova, J. Zimmerberg, Lipid polymorphisms and membrane shape. *Cold Spring Harb. Perspect. Biol.* **3**, a004747 (2011).
14. S. Vanni, H. Hirose, H. Barelli, B. Antonny, R. Gautier, A sub-nanometre view of how membrane curvature and composition modulate lipid packing and protein recruitment. *Nat. Commun.* **5**, 4916 (2014).
15. P. Bassereau *et al*., The 2018 biomembrane curvature and remodeling roadmap. *J. Phys. D Appl. Phys.* **51**, 343001 (2018).
16. E. Layre *et al*., A comparative lipidomics platform for chemotaxonomic analysis of Mycobacterium tuberculosis. *Chem. Biol.* **18**, 1537–1549 (2011).
17. M. Jain *et al*., Lipidomics reveals control of Mycobacterium tuberculosis virulence lipids via metabolic coupling. *Proc. Natl. Acad. Sci. U.S.A.* **104**, 5133–5138 (2007).
18. G. Sulzenbacher *et al*., LppX is a lipoprotein required for the translocation of phthiocerol dimycocerosates to the surface of Mycobacterium tuberculosis. *EMBO J.* **25**, 1436–1444 (2006).
19. S. J. Marrink, D. P. Tieleman, Perspective on the Martini model. *Chem. Soc. Rev.* **42**, 6801–6822 (2013).
20. H. I. Ingólfsson, C. Arnarez, X. Periole, S. J. Marrink Computational "microscopy" of cellular membranes. *J. Cell Sci.* **129**, 257–268 (2016).
21. H. Khandelia, L. Duelund, K. I. Pakkanen, J. H. Ipsen, Triglyceride blisters in lipid bilayers: Implications for lipid droplet biogenesis and the mobile lipid signal in cancer cell membranes. *PLoS One* **5**, e12811 (2010).
22. K. Ben M'barek *et al*., ER membrane phospholipids and surface tension control cellular lipid droplet formation. *Dev. Cell* **41**, 591–604.e7 (2017).
23. J. M. Seddon, Structure of the inverted hexagonal (HII) phase, and non-lamellar phase transitions of lipids. *Biochim. Biophys. Acta* **1031**, 1–69 (1990).
24. F. Separovic, K. Gawrisch, Effect of unsaturation on the chain order of phosphatidylcholines in a dioleoylphosphatidylethanolamine matrix. *Biophys. J.* **71**, 274–282 (1996).
25. N. Fuller, R. P. Rand, The influence of lysolipids on the spontaneous curvature and bending elasticity of phospholipid membranes. *Biophys. J.* **81**, 243–254 (2001).
26. E. E. Kooijman *et al*., Spontaneous curvature of phosphatidic acid and lysophosphatidic acid. *Biochemistry* **44**, 2097–2102 (2005).
27. S.-J. Marrink, A. E. Mark, Molecular view of hexagonal phase formation in phospholipid membranes. *Biophys. J.* **87**, 3894–3900 (2004).
28. J. C. Shelley *et al*., Simulations of phospholipids using a coarse grain model. *J. Phys. Chem. B* **105**, 9785–9792 (2001).
29. W. Shinoda, R. DeVane, M. L. Klein, Coarse-grained molecular modeling of non-ionic surfactant self-assembly. *Soft Matter* **4**, 2454–2462 (2008).
30. M. L. Klein, W. Shinoda, Large-scale molecular dynamics simulations of self-assembling systems. *Science* **321**, 798–800 (2008).
31. P. R. Cullis, B. de Kruijff, Lipid polymorphism and the functional roles of lipids in biological membranes. *Biochim. Biophys. Acta* **559**, 399–420 (1979).
32. A. Roux *et al*., Role of curvature and phase transition in lipid sorting and fission of membrane tubules. *EMBO J.* **24**, 1537–1545 (2005).
33. B. Sorre *et al*., Curvature-driven lipid sorting needs proximity to a demixing point and is aided by proteins. *Proc. Natl. Acad. Sci. U.S.A.* **106**, 5622–5626 (2009).
34. P. L. Yeagle, F. T. Smith, J. E. Young, T. D. Flanagan, Inhibition of membrane fusion by lysophosphatidylcholine. *Biochemistry* **33**, 1820–1827 (1994).
35. S. J. Marrink, A. E. Mark, The mechanism of vesicle fusion as revealed by molecular dynamics simulations. *J. Am. Chem. Soc.* **125**, 11144–11145 (2003).
36. S. Sahu, W. S. Lynn, Lipid composition of human alveolar macrophages. *Inflammation* **2**, 83–91 (1977).
37. M. Rappolt, A. Hickel, F. Bringezu, K. Lohner, Mechanism of the lamellar/inverse hexagonal phase transition examined by high resolution x-ray diffraction. *Biophys. J.* **84**, 3111–3122 (2003).
38. C. Tilcock, P. R. Cullis, The polymorphic phase-behavior and miscibility properties of synthetic phosphatidylethanolamines. *Biochim. Biophys. Acta* **684**, 212–218 (1982).
39. V. Le Cabec, C. Cols, I. Maridonneau-Parini, Nonopsonic phagocytosis of zymosan and Mycobacterium kansasii by CR3 (CD11b/CD18) involves distinct molecular determinants and is or is not coupled with NADPH oxidase activation. *Infect. Immun.* **68**, 4736–4745 (2000).
40. E. Rhoades *et al*., Identification and macrophage-activating activity of glycolipids released from intracellular Mycobacterium bovis BCG. *Mol. Microbiol.* **48**, 875–888 (2003).
41. J. T. Crowley *et al*., Lipid exchange between Borrelia burgdorferi and host cells. *PLoS Pathog.* **9**, e1003109 (2013).

Downloaded at UNIVERSITAT MUENCHEN Bibliothek Bereich Physiologie on November 24, 2019

42. L. Brown, J. M. Wolf, R. Prados-Rosales, A. Casadevall, Through the wall: Extracellular vesicles in Gram-positive bacteria, mycobacteria and fungi. *Nat. Rev. Microbiol.* **13**, 620–630 (2015).
43. J. M. Bomberger *et al*., Long-distance delivery of bacterial virulence factors by Pseudomonas aeruginosa outer membrane vesicles. *PLoS Pathog.* **5**, e1000382 (2009).
44. L. V. Chernomordik, M. M. Kozlov, Mechanics of membrane fusion. *Nat. Struct. Mol. Biol.* **15**, 675–683 (2008).
45. M. Zick, C. Stroupe, A. Orr, D. Douville, W. T. Wickner, Membranes linked by trans-SNARE complexes require lipids prone to non-bilayer structure for progression to fusion. *eLife* **3**, e01879 (2014).
46. P. Campomanes, V. Zoni, S. Vanni, Local accumulation of diacylglycerol alters membrane properties nonlinearly due to its transbilayer activity. *Commun. Chem.* **2**, 1–8 (2019).
47. A. Bacle, R. Gautier, C. L. Jackson, P. F. J. Fuchs, S. Vanni, Interdigitation between triglycerides and lipids modulates surface properties of lipid droplets. *Biophys. J.* **112**, 1417–1430 (2017).
48. F. N. Barrera, J. Fendos, D. M. Engelman, Membrane physical properties influence transmembrane helix formation. *Proc. Natl. Acad. Sci. U.S.A.* **109**, 14422–14427 (2012).
49. C. J. B. daCosta, L. Dey, J. P. D. Therien, J. E. Baenziger, A distinct mechanism for activating uncoupled nicotinic acetylcholine receptors. *Nat. Chem. Biol.* **9**, 701–707 (2013).
50. C. Pliotas *et al*., The role of lipids in mechanosensation. *Nat. Struct. Mol. Biol.* **22**, 991–998 (2015).
51. R. C. Hresko, T. E. Kraft, A. Quigley, E. P. Carpenter, P. W. Hruz, Mammalian glucose transporter activity is dependent upon anionic and conical phospholipids. *J. Biol. Chem.* **291**, 17271–17282 (2016).
52. D. P. Speert, S. C. Silverstein, Phagocytosis of unopsonized zymosan by human monocyte-derived macrophages: Maturation and inhibition by mannan. *J. Leukoc. Biol.* **38**, 655–658 (1985).
53. K. R. Rosholm *et al*., Membrane curvature regulates ligand-specific membrane sorting of GPCRs in living cells. *Nat. Chem. Biol.* **13**, 724–729 (2017).
54. S. Aimon *et al*., Membrane shape modulates transmembrane protein distribution. *Dev. Cell* **28**, 212–218 (2014).
55. P. J. Hamilton *et al*., PIP2 regulates psychostimulant behaviors through its interaction with a membrane protein. *Nat. Chem. Biol.* **10**, 582–589 (2014).
56. T. Hirama *et al*., Membrane curvature induced by proximity of anionic phospholipids can initiate endocytosis. *Nat. Commun.* **8**, 1393 (2017).
57. C. H. Liu, H. Liu, B. Ge, Innate immunity in tuberculosis: host defense vs pathogen evasion. *Cell. Mol. Immunol.* **14**, 963–975 (2017).
58. J. Augenstreich *et al*., ESX-1 and phthiocerol dimycocerosates of Mycobacterium tuberculosis act in concert to cause phagosomal rupture and host cell apoptosis. *Cell. Microbiol.* **19**, e12726 (2017).
59. J. Quigley *et al*., The cell wall lipid PDIM contributes to phagosomal escape and host cell exit of *Mycobacterium tuberculosis*. *MBio* **8**, e00148-17. (2017).
60. R. Guler, F. Brombacher, Host-directed drug therapy for tuberculosis. *Nat. Chem. Biol.* **11**, 748–751 (2015).
61. G. P. Holland, S. K. McIntyre, T. M. Alam, Distinguishing individual lipid headgroup mobility and phase transitions in raft-forming lipid mixtures with 31P MAS NMR. *Biophys. J.* **90**, 4248–4260 (2006).
62. P. R. Cullis, B. De Kruijff, Polymorphic phase behaviour of lipid mixtures as detected by 31P NMR. Evidence that cholesterol may destabilize bilayer structure in membrane systems containing phosphatidylethanolamine. *Biochim. Biophys. Acta* **507**, 207–218 (1978).
63. L. Moran, N. Janes, Tracking phospholipid populations in polymorphism by sideband analyses of 31P magic angle spinning NMR. *Biophys. J.* **75**, 867–879 (1998).
64. R. Salomon Ferrer, D. A. Case, R. C. Walker, An overview of the Amber biomolecular simulation package. *Wiley Interdiscip. Rev. Comput. Mol. Sci.* **3**, 198–210 (2012).
65. C. J. Dickson *et al*., Lipid14: The amber lipid force field. *J. Chem. Theory Comput.* **10**, 865–879 (2014).
66. J. Wang, R. M. Wolf, J. W. Caldwell, P. A. Kollman, D. A. Case, Development and testing of a general amber force field. *J. Comput. Chem.* **25**, 1157–1174 (2004).
67. E. L. Wu *et al*., CHARMM-GUI Membrane Builder toward realistic biological membrane simulations. *J. Comput. Chem.* **35**, 1997–2004 (2014).
68. S. Jo, T. Kim, V. G. Iyer, W. Im, CHARMM-GUI: A web-based graphical user interface for CHARMM. *J. Comput. Chem.* **29**, 1859–1865 (2008).
69. M. J. Abraham *et al*., GROMACS: High performance molecular simulations through multi-level parallelism from laptops to supercomputers. *SoftwareX* **1-2**, 19–25 (2015).
70. D. H. de Jong *et al*., Improved parameters for the Martini coarse-grained protein force field. *J. Chem. Theory Comput.* **9**, 687–697 (2013).
71. S. J. Marrink, A. H. de Vries, A. E. Mark, Coarse grained model for semiquantitative lipid simulations. *J. Phys. Chem. B* **108**, 750–760 (2004).
72. S. J. Marrink, H. J. Risselada, S. Yefimov, D. P. Tieleman, A. H. de Vries, The MARTINI force field: Coarse grained model for biomolecular simulations. *J. Phys. Chem. B* **111**, 7812–7824 (2007).
73. Y. Qi *et al*., CHARMM-GUI Martini maker for coarse-grained simulations with the Martini force field. *J. Chem. Theory Comput.* **11**, 4486–4494 (2015).
74. M. Parrinello, A. Rahman, Polymorphic transitions in single crystals: A new molecular dynamics method. *J. Appl. Phys.* **52**, 7182 (1981).
75. G. Bussi, D. Donadio, M. Parrinello, Canonical sampling through velocity rescaling. *J. Chem. Phys.* **126**, 014101 (2007).
76. H. Berendsen, J. Postma, W. F. Vangunsteren, A. DiNola, J. R. Haak, Molecular-dynamics with coupling to an external bath. *J. Chem. Phys.* **81**, 3684–3690 (1984).
77. W. Humphrey, A. Dalke, K. Schulten, VMD: Visual molecular dynamics. *J. Mol. Graph.* **14**, 33–38 (1996).

Downloaded at UNIVERSITAT MUENCHEN Bibliothek Bereich Physiologie on November 24, 2019